Mesospheric temperatures and sodium properties measured with the ALOMAR Na lidar compared with WACCM

Tim Dunker [a,*], Ulf-Peter Hoppe [a], Wuhu Feng [b,c], John M.C. Plane [b], Daniel R. Marsh [d]

[a] Department of Physics and Technology, University of Tromsø - The Arctic University of Norway, 9037 Tromsø, Norway
[b] School of Chemistry, University of Leeds, Leeds LS2 9JT, UK
[c] School of Earth and Environment, University of Leeds, Leeds LS2 9JT, UK
[d] Atmospheric Chemistry Division, National Center for Atmospheric Research, PO Box 3000, Boulder, CO 8030-3000, USA

ABSTRACT

We present a comparison of the temperature and sodium layer properties observed by the ALOMAR Na lidar (69.3°N, 16.0°E) and simulated by the Whole Atmosphere Community Climate Model with specified dynamics and implemented sodium chemistry (WACCM-Na). To constrain the meteorological fields below 60 km, we use MERRA and GEOS-5. For the years 2008 to 2012, we analyse daily averages of temperature between 80.5 km and 101.5 km altitude, and of the Na layer's peak height, peak density, and centroid height. Both model runs are able to reproduce the pronounced seasonal cycle of Na number density and temperature at high latitudes very well. Especially between 86.5 km and 95.5 km, the measured and simulated temperatures agree very well. The lidar measurements confirm the model predictions that the January 2012 stratospheric warming led to large variation in temperature and Na density. The correlation coefficient between Na number density and temperature is positive for almost all altitudes in the lidar data, but not in the simulations. On average, the centroid height and peak height measured by lidar is about 2 km–3 km higher than simulated by WACCM-Na.

1. Introduction

In 1929, Slipher observed the Na D lines in the spectrum of the night sky (Slipher, 1929). It has subsequently been established that a mesospheric layer of Na is the source of that emission. The mesospheric metal layers have been known for many decades now, but many of the phenomena and mechanisms involved remain less than well understood. Ground-based lidar measurements and sounding rocket campaigns (Bowman et al., 1969; Gibson et al., 1979; Fricke and von Zahn, 1985; Lübken and von Zahn, 1991) revealed details both about the thermal structure of the mesopause region, and the region's ion composition (Kopp, 1997). However, such measurements are limited in time and space, especially at high latitudes. Laboratory studies (Plane et al., 2002, and references therein) have greatly advanced the understanding of the metal chemistry, and have contributed to the development of sophisticated models of the mesospheric metal layers (Plane et al., 1999; Gerding et al., 2000; Plane, 2004; Marsh et al., 2013a; Feng et al., 2013). A comparison of temperature and wind speeds measured by lidar with, among other models, version 3 of the

Whole Atmosphere Community Climate Model (WACCM) has been published by Yuan et al. (2008).

Recently, mesospheric sodium chemistry has been implemented in WACCM, version 4, by Marsh et al. (2013a), using the sodium (Na) chemistry scheme of Plane (2004) and a seasonally varying meteoric injection rate of Na at different latitudes and altitudes.

The origin of mesospheric sodium is meteoric ablation (Junge et al., 1962; Clemesha et al., 1978). Differential ablation of meteoric metals has been modelled by Vondrak et al. (2008). The estimates of the total meteoric influx (Plane, 2012, and references therein) vary over a range of two orders of magnitude ($O \sim 1$–100 t d^{-1}).

The influx varies with latitude and season (e.g. Fig. 1 in Marsh et al., 2013a). The combination of meteoric influx and eddy diffusion puts constraints on the sodium abundance. For the model we use in this study, as in Marsh et al. (2013a), the total meteoric influx has been assumed as 4.6 t d^{-1}. The Prandtl number is defined as the dimensionless ratio of kinematic viscosity to thermal diffusivity, and has been set to $Pr=4$.

In Arctic summer, temperatures in the upper mesosphere get sufficiently cold ($T \lesssim 150$ K) for ice particles to form (Lübken, 1999). Sodium bicarbonate molecules, which are the major reservoir species of sodium below about 85 km, can act as condensation nuclei for ice particles (Plane, 2000). The formation of

* Corresponding author.
    E-mail address: tim.dunker@uit.no (T. Dunker).

ice particles on $NaHCO_3$ condensation nuclei lower the Na number density between 80 and 90 km, whenever the temperature is lower than 140 K (Plane, 2000).

We update some of the results by Marsh et al. (2013a) using two meteorological analyses when we constrain the model at lower altitudes. We compare data from the ALOMAR Na lidar, located at the ALOMAR observatory on the Norwegian island Andøya (69°N, 16°E), with WACCM-Na results for the period 2008–2012. We have performed two nearly identical runs of WACCM-Na (see Section 2.2). This comparison is an addition to Marsh et al. (2013a), who include high-latitude data from the southern hemisphere. We compare diurnally averaged sodium lidar temperatures at different altitudes with WACCM-Na's simulated temperatures. The observed Na layer peak height, centroid height, peak density, and column density are also compared to WACCM-Na simulations as daily averages.

Section 2 gives a brief overview of the methods used for this paper. We present our results in Section 3. Sections 4 and 5 consist of a discussion and conclusions, respectively.

2. Methods

2.1. ALOMAR Na lidar

The ALOMAR Na lidar is a resonance fluorescence lidar that probes the mesospheric Na layer (Arnold and She, 2003), employing techniques that Fricke and von Zahn (1985) have described. It has been in operation since August 2000, and is capable of daylight measurements. The system has recently been described by Dunker et al. (2013) for measurements in darkness. Here, we will only give a brief overview of the measurement principle, and describe the necessary changes for measurements in daylight.

The lidar emits pulses of 7 ns (full width at half maximum, FWHM) at $\lambda = 589$ nm light, with a repetition rate of 50 Hz. Continuous-wave light at 589 nm is created through sum-frequency generation of two infrared lasers (1064 nm and 1319 nm) in a periodically poled Lithium Niobate crystal (Nishikawa et al., 2009). The wavelength is tuned to the D_{2a} Lamb dip of the sodium D_2 line, where the resonant scattering cross section is largest. A pump laser at 532 nm amplifies the continuous-wave light in a dye amplifier, creating 7 ns pulses of 589 nm light at 50 Hz with an energy of about 10–20 mJ. The backscattered photons from the atmospheric sodium layer are received by telescopes with a diameter of 1.8 m (von Zahn et al., 2000). The field of view is 600 µrad, the laser beam divergence 450 µrad (full angle; corresponds to a beam diameter of 45 m at 100 km altitude). The received photons are guided in fibres from the telescopes to a chopper.

In darkness, the backscattered photons pass through a band-pass interference filter (centred at 589 nm, and a FWHM of 1 nm) before they are received by photon-counting photomultiplier tubes.

In daylight, i.e. when the solar zenith angle is smaller than about 96°, the receiver setup needs to be changed in order to reduce the solar background as much as possible. We use Faraday anomalous dispersion optical filters (FADOF). Such filters have been described by Chen et al. (1996) and Harrell et al. (2009), for example. In the case of sodium, a FADOF consists of a heated sodium vapour cell surrounded by a magnet, which creates an axial magnetic field. In addition, there is one polarizer in front of and one behind the sodium vapour cell. These are crossed to each other. The combination of the axial magnetic field and the vapour density in the Na cell is chosen such that the Faraday rotation becomes exactly 90°. Behind the FADOF, the same setup as in darkness (see above) is used. When a photon with a wavelength of

589 nm passes through the first polarizer and enters the vapour cell, the axial magnetic field rotates the polarisation plane (Faraday rotation) by 90°, such that it is transmitted through the second polarizer and can be detected by a photomultiplier tube. When a photon of a different wavelength enters the sodium vapour cell, it will not be subject to Faraday rotation, and subsequently it cannot pass through the second polarizer. The use of a FADOF leads to a reduction of the solar background, typically $O \sim 10^{-5}$ (Chen et al., 1993), maintaining a sufficient signal-to-noise ratio at $\lambda = 589$ nm even in daylight.

The Na atoms in the atmosphere follow a Maxwellian velocity distribution according to the ambient temperature, which leads to a temperature-dependent Doppler broadening of the resonant absorption (e.g. Fricke and von Zahn, 1985). Therefore, the lidar has been designed to emit three wavelengths in a cycle of five seconds each: at the D_{2a} frequency, and one each at ± 630 MHz relative to the D_{2a} frequency. Each such cycle probes the Doppler broadening of the Na D_2 line, thus enabling temperature measurements.

The vertical resolution of the lidar data in this study is 1.5 km. Reported temperatures for any altitude z are therefore average temperatures of the altitude interval $z \pm 0.75$ km.

The Na density is calculated according to Fricke and von Zahn (1985, Eq. (9)). The uncertainty of the Na density is dominated by the stratospheric air density uncertainty, which we estimate to be within $\pm 10\%$.

In darkness, the temperature uncertainty at the Na layer peak altitude is typically around 2 K, and up to 15 K at the layer edges, at a temporal resolution of five minutes. In daylight, the respective measurement uncertainties are typically $\Delta T < 8$ K and $\Delta n_{Na} < 10^8$ m^{-3}. The temperature uncertainty depends on the signal-to-noise ratio, and thus on the Na number density. Given an Na number density large enough in summer, ΔT can be as small as 2 K at peak layer altitudes.

Data analysis has been described by Heinrich (2008) and Kaifler (2009).

2.2. Whole Atmosphere Community Climate Model

We use the Whole Atmosphere Community Climate Model, version 4 with specified dynamics. Here, we have performed two similar runs, where the model's fields are constrained to the meteorological fields from either NASA's Goddard Earth Observing System Model, Version 5 (GEOS-5), or from NASA's Modern-Era Retrospective Analysis for Research and Applications (MERRA) (Lamarque et al., 2012; Rienecker et al., 2011). For simplicity, we term these WACCM-Na simulations "WACCM(GEOS-5)" and "WACCM(MERRA)" in the following.

The meteorological fields simulated by WACCM-Na are constrained to the reanalysis product according to Eq. (1), which describes the nudging for the temperature T:

$$T = \alpha \cdot T_r + (1 - \alpha) \cdot T_{WACCM}, \qquad (1)$$

where α is a nudging factor, T_r is the temperature obtained from GEOS-5 or MERRA reanalyses, and T_{WACCM} is the temperature calculated by WACCM-Na without constraints. For altitudes between 15 and 50 km, we use $\alpha = 0.01$. From 50 km upwards, the nudging factor decreases linearly to $\alpha = 0$ at 60 km and above. The model's time step is 30 min. At each altitude and each time step, the model temperature, zonal and meridional winds are nudged in the way described by Eq. (1).

The resolution is 2.5° in longitude, and 1.9° in latitude. WACCM-Na has 88 vertical pressure levels, with a topmost level of 5.1×10^{-6} hPa, which corresponds roughly to 140 km. At mesospheric altitudes, the vertical resolution is two grid points per

scale height, which is approximately 3.5 km. The vertical profiles have been interpolated to yield an equidistant 1 km grid by converting the geopotential height field to geometric height.

The sodium chemistry scheme is based on Plane (2004), and was implemented into WACCM by Marsh et al. (2013a). They have provided a detailed description of the implemented chemistry and the meteoroid input function: from a repeating climatology, a global ablated mass input of 4.6 t d⁻¹ is prescribed, of which 0.8% (0.035 t d⁻¹) is sodium.

The current WACCM-Na version has been described by Marsh et al. (2013b), including recent improvements and the various forcing mechanisms. For instance, the quasi-biennial oscillation is accounted for using the approach reported by Matthes et al. (2010). Ionospheric E region chemistry is included in WACCM-Na, as is particle precipitation in the auroral regions. Species like HO_x and NO_x, which can be produced or depleted through an increase or decrease of solar irradiance (Jackman et al., 2008), are included in the model. The loss of sodium through the uptake on meteoric smoke particles is simulated by a catalytic reaction involving sodium bicarbonate ($NaHCO_3$), which eventually leads to dimerisation and loss (Plane, 2004; Marsh et al., 2013a). Electrodynamics is not included in the current WACCM-Na version (Feng et al., 2013).

Reanalysis data from GEOS-5 and MERRA is available every six hours, beginning at 00:00 UTC. The model calculates atmospheric sodium number densities and temperatures every 30 min, and interpolates the meteorological fields from GEOS-5 (or MERRA, respectively) to match WACCM-Na's output time interval of 30 min.

The WACCM-Na run nudged to GEOS-5 covers the time period from 2 January 2004 to 10 March 2012, while the run nudged to MERRA covers the period from 2 January 2004 to 26 December 2010. Apart from the slightly different time periods covered and the different reanalysis product used for the nudging, the runs are identical. Here, we concentrate on the time from 1 January 2008 to the end of each run.

Even though WACCM-Na is a global 3D model, we only use the simulated geophysical results for the geographic coordinates 69°N and 16°E, which are approximately the location of the ALOMAR observatory.

3. Results

For this comparison, we chose only measurements that lasted for more than one hour. In total, 81 days with a total measurement time of about 379 h have been analysed. Fig. 1 shows the histogram of lidar measurement durations for this study, and number of measurements per month. The mean measurement duration is 4.7 h. Sporadic Na layers have not been removed from the lidar

Table 1
Mean temperatures $\overline{T} \pm 2\sigma$ (K) for the altitude from 80.5 km to 101.5 km and for whole time period, simulated by the two WACCM-Na runs and measured by the ALOMAR Na lidar.

Altitude (km)	WACCM-Na nudged to		ALOMAR
	GEOS-5 $\overline{T} \pm 2\sigma$ (K)	MERRA	Na lidar
80.5	192.5 ± 1.2	192.7 ± 1.2	227.5 ± 4.5
83.5	193.7 ± 1.2	194.6 ± 1.2	212.6 ± 11.0
86.5	196.0 ± 1.2	197.5 ± 1.2	199.6 ± 12.4
89.5	197.5 ± 1.1	198.6 ± 1.1	194.3 ± 12.5
92.5	198.2 ± 1.1	197.9 ± 1.1	195.4 ± 8.1
95.5	201.5 ± 1.2	199.3 ± 1.2	204.3 ± 5.1
98.5	211.1 ± 1.4	206.5 ± 1.4	209.1 ± 6.2
101.5	228.0 ± 1.7	221.0 ± 1.7	215.6 ± 7.7

data (see also Section 3.1.2, and Figs. 4 and 7).

Times are given in universal time (UT). On Andøya, local time is UT minus two hours in summer, and UT minus one hour in winter.

3.1. Daily averages

All values presented in this section are daily averages. The error of any daily mean quantity measured by lidar is calculated as the standard error σ, i.e.

$$\sigma = \frac{s}{\sqrt{N}},$$

where s is the standard deviation of the respective time series, and N is the number of individual measurements. Exceptions from this rule are stated explicitly.

Mean values of lidar measurements given in Tables 1 and 3 have been computed from monthly mean values. This avoids a potential bias towards winter months, which are better covered by lidar measurements (see Fig. 1, right panel). At 80.5 km, the reported value in Table 1 is based on nine monthly mean profiles. For May, June, and July, no measurements are available at that altitude.

3.1.1. Mesospheric temperatures

The vertical resolution of the Na lidar data is 1.5 km. Therefore, any measured temperature that is reported here is the average of such an altitude range.

Fig. 2 shows daily averages of modelled and observed temperatures for altitudes from 80.5 to 101.5 km in steps of 3 km. The 2σ scatter range of the WACCM-Na simulations is not shown due to the scale: for both WACCM-Na runs, the 2σ scatter ranges lie between ± 1.1 K and ± 2.2 K for the altitudes shown. The 2σ scatter range, which is related to the geophysical variability at the respective altitude, is smallest at 95.5 km, and increases above and
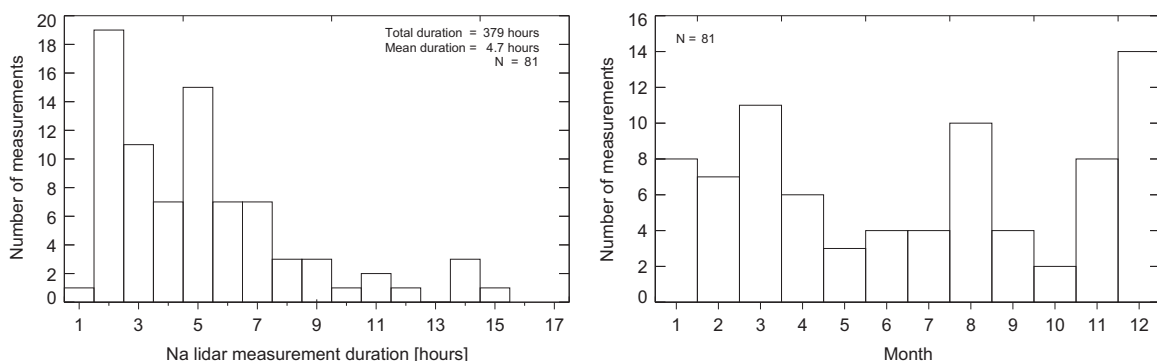
Fig. 1. Left panel: Histogram of the individual lidar measurement durations (81 individual measurements in total) between 1 January 2008 and 20 March 2012. The bin size is one hour. Mean measurement duration: 4.7 h. Total measurement time: ~379 h. Right panel: number of measurements per month.
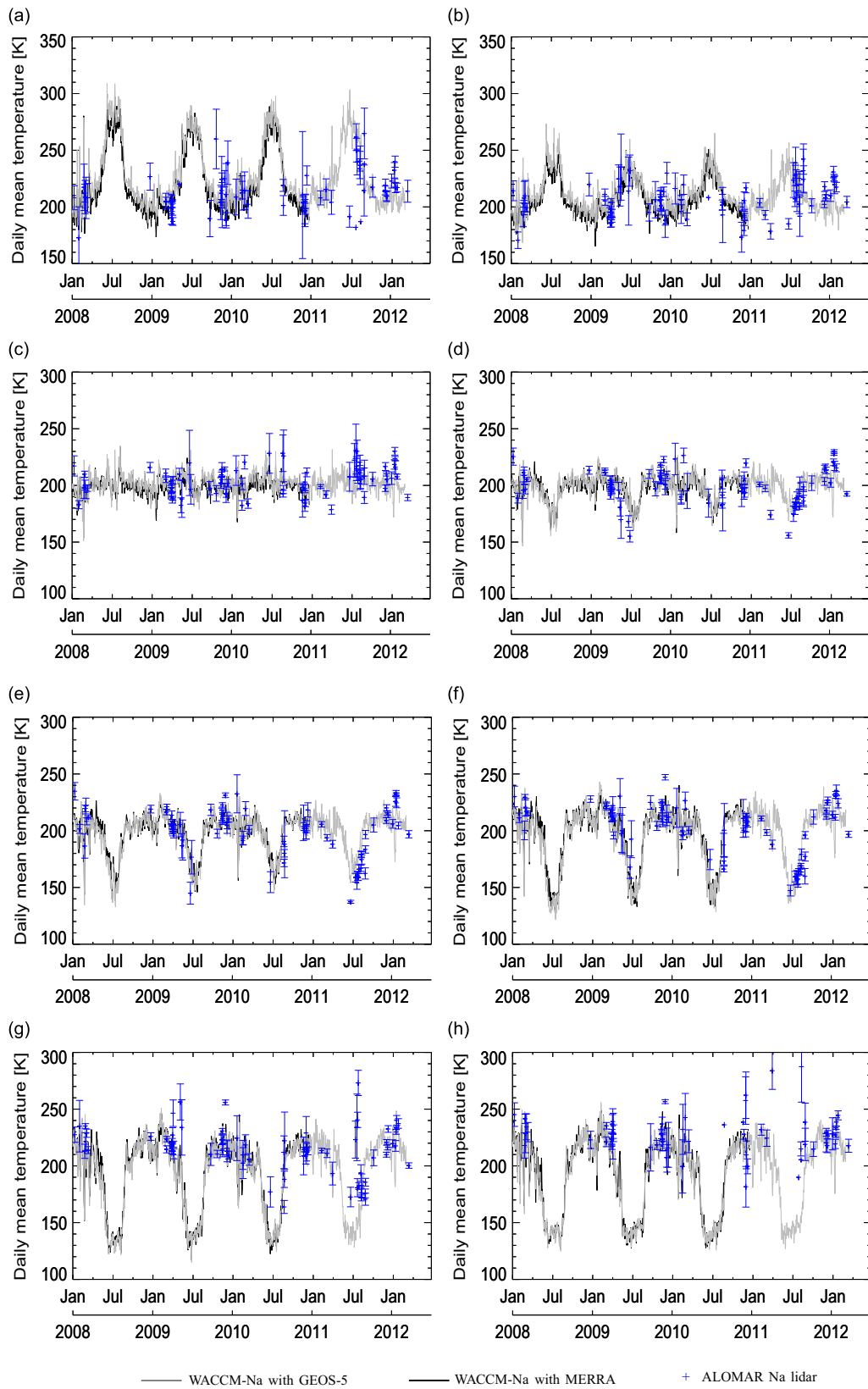
Fig. 2. Time series of daily averaged temperatures at altitudes of 80.5 km to 101.5 km in steps of 3 km (see panel captions) for the period of 1 January 2008 to 20 March 2012. Note the different temperature scales. Grey solid line: Modelled temperatures from WACCM-Na nudged to GEOS-5. Black solid line: Modelled temperatures from WACCM-Na nudged to MERRA. Blue: Temperatures measured by Na lidar. The error bars indicate the 2σ range. Altitudes: (a) 101.5 km; (b) 98.5 km; (c) 95.5 km; (d) 92.5 km; (e) 89.5 km; (f) 86.5 km; (g) 83.5 km; and (h) 80.5 km. (For interpretation of the references to color in this figure caption, the reader is referred to the web version of this article.)
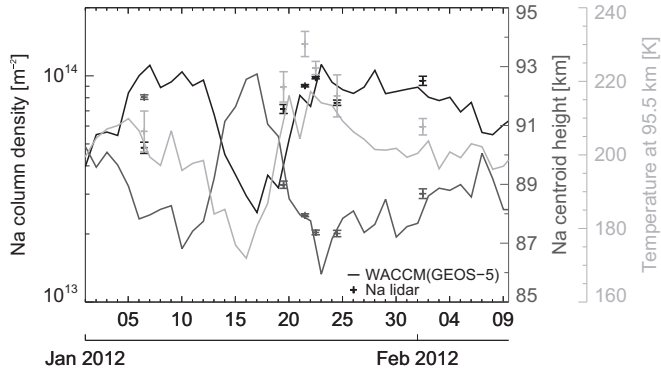
Fig. 3. Diurnal averages of the Na column density in m⁻² (black), Na layer centroid height in km (dark grey), and temperature at 95.5 km (light grey) for the time period from 1 January 2012 to 9 February 2012. Solid lines: data from WACCM (GEOS-5); plus signs: data from the ALOMAR Na lidar. The error bars indicate the 2σ range.

below that height. This is due to the increasing strength of the seasonal cycle.

A striking feature is the absence of a pronounced seasonal cycle at 95.5 km. However, the effects of intermittent events, like the sudden stratospheric warming in January 2012, are evident in WACCM-Na and lidar data (Fig. 3). Chandran et al. (2014, Table 1) characterised that event as a minor stratospheric warming, followed by the formation of an elevated stratopause. For the period from 1 January 2012 to 9 February 2012, Fig. 3 shows mesospheric temperatures at 95.5 km altitude, the Na layer centroid height, and Na column density. There is no lidar data available during the sudden stratospheric warming, but for the days immediately after. The model shows a pronounced cooling at 95.5 km, and a simultaneous decrease of Na column density, while the layer moves upward by about 5 km. After 17 January 2012, the temperature and the column density increase again, while the layer moves downward. The temperature is even higher than it was before the onset of the mesospheric cooling. Lidar measurements confirm the increase in temperature and column density. There is no apparent large variation of the properties due to the solar proton event on 23/24 January 2012.

Above about 95 km, the seasonal cycle is reversed, and the strength of the seasonal cycle increases with increasing altitude. This is consistent with the lidar data, despite being sparse in summer months. An observational difficulty is the narrow Na layer in summer: temperature measurements are hardly possible at altitudes higher than about 97 km due to the very low Na density at those altitudes. The relatively low signal-to-noise ratio leads to increased temperature uncertainties. Additionally, the influence of tidal waves is large, leading to a high degree of geophysical variability.

Modelled temperatures by WACCM-Na and measured temperatures by lidar agree to a certain extent. The agreement is best in 2011 and 2012, while there are differences of up to 50 K in autumn 2009, but these occur at the Na layer boundaries and thus carry a large uncertainty due to the low signal-to-noise ratio at those altitudes. The same is true for the apparently large differences at several altitudes in summer 2011.

We have summarised the mean temperatures for each altitude in Table 1. In winter (December, January, February), the average temperature of the minimum in each day's profile $T(z)$ is warmer by about 6 K–10 K in the WACCM-Na simulations compared to lidar measurements (Table 2). The altitude at which the minimum occurs is roughly equal in simulations and measurements.

3.1.2. Na column density and peak density

Diurnal mean values of Na column density are shown in Fig. 4.

Table 2
Average winter (December, January, February) temperature $\overline{T_{min}}$ of the minimum in each day's profile $T(z)$, and the average of the corresponding altitude $\bar{z}$ of that temperature minimum.

Data set	$\overline{T_{min}} \pm 2\sigma$ (K)	$\bar{z} \pm 2\sigma$ (km)
WACCM(GEOS-5)	192.5 $\pm$ 1.0	94.7 $\pm$ 0.5
WACCM(MERRA)	187.5 $\pm$ 1.3	95.7 $\pm$ 0.7
ALOMAR Na lidar	181.8 $\pm$ 6.6	96.3 $\pm$ 1.2

The standard errors of the column density simulated by WACCM-Na are not shown, because they are an order of magnitude smaller than the expectation value (average 2σ: $\pm 1.5 \times 10^{12}$ m⁻² for WACCM(GEOS-5); WACCM(MERRA): $\pm 1.3 \times 10^{12}$ m⁻²).

The pronounced seasonal cycle is visible in lidar and WACCM-Na data, even though the lidar data are rather sparse in summer months. One of the striking features in Fig. 4 is that both WACCM-Na runs reveal a rather rapid transition from the summer to the winter state. The transition from winter to summer occurs slower: the column density decreases until the end of March, reaching a local minimum, before slightly increasing in April/May, followed by a rapid decrease towards an annual minimum in June and July. However, this behaviour is not very distinct in 2008 compared to the other years.

The largest mean column density is simulated by the WACCM (GEOS-5) run, though not continuously. In summer 2008, the Na column density is larger in the WACCM(MERRA) simulation. On average, the Na column density measured by lidar is smaller than in both simulations, while the peak densities are in better agreement (Table 3).

The difference between summer and winter Na column density is more than an order of magnitude, which is similar to what Marsh et al. (2013a) found. At 69°N, the annual variation is as strong as at the South Pole.

The daily averages of the Na peak density, i.e. the maximum Na density of the whole layer, are shown in Fig. 5. The standard errors of WACCM-Na's simulated peak densities are not shown in Fig. 5, because these are an order of magnitude smaller than the expectation value (average 2σ: $\pm 1.1 \times 10^8$ m⁻³ for WACCM(GEOS-5); WACCM(MERRA): $\pm 1.0 \times 10^8$ m⁻³).

Sometimes the lidar measured larger densities than simulated by the two WACCM-Na runs, sometimes it is the other way around. A notable outlier is 28 June 2009, due to a large sporadic Na layer measured by the lidar. The agreement is especially good in 2011 and 2012, even in summer months despite sparse data.

3.1.3. Correlation between Na density and temperature

In Fig. 6, we show the Pearson correlation coefficient between Na density and temperature for each of the three data sets. The Pearson correlation coefficient assumes a linear relationship between the two quantities it is applied to, in this case neutral temperature and Na number density. Regarding the correlation

Table 3
Mean Na layer column density, peak density, peak height, and centroid height simulated by the two WACCM-Na runs and measured by the ALOMAR Na lidar. All values are mean values $\pm$ standard deviation.

Mean Na layer property	WACCM-Na nudged to		ALOMAR
	GEOS-5	MERRA	Na lidar
Column density (10^{13} m⁻²)	4.4 $\pm$ 2.4	3.9 $\pm$ 2.0	3.5 $\pm$ 1.3
Peak density (10^9 m⁻³)	3.8 $\pm$ 1.6	3.3 $\pm$ 1.3	3.6 $\pm$ 1.4
Peak height (km)	88.1 $\pm$ 1.9	87.8 $\pm$ 1.9	91.8 $\pm$ 1.3
Centroid height (km)	89.3 $\pm$ 1.2	89.3 $\pm$ 1.2	91.6 $\pm$ 1.1
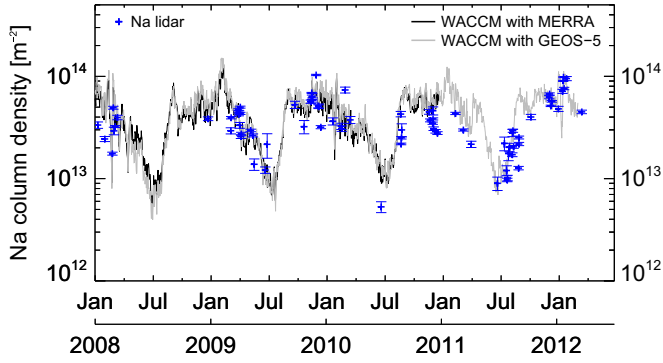
Fig. 4. Diurnally averaged Na column density in m^{-2}. Grey solid line: Modelled column densities from WACCM-Na nudged to GEOS-5. Black solid line: Modelled column densities from WACCM-Na nudged to MERRA. Blue: Column densities measured by Na lidar. The error bars indicate the 2σ range. (For interpretation of the references to color in this figure caption, the reader is referred to the web version of this article.)
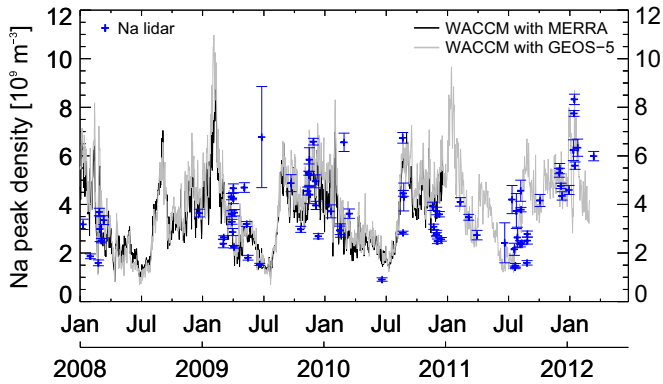
Fig. 5. Diurnal averages of the Na layer peak density in 10^9 m^{-3}. Grey solid line: Modelled peak density from WACCM-Na nudged to GEOS-5. Black solid line: Modelled peak density from WACCM-Na nudged to MERRA. Blue: Peak density measured by Na lidar. The error bars indicate the 2σ range. (For interpretation of the references to color in this figure caption, the reader is referred to the web version of this article.)
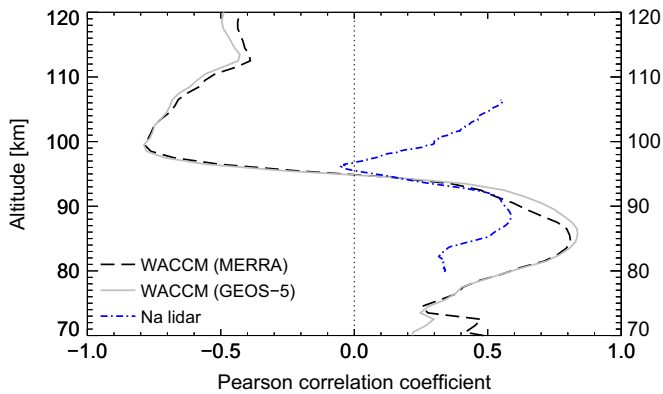

Fig. 6. Pearson correlation coefficient between diurnally averaged Na number density and temperature versus altitude in km. Grey solid line: WACCM-Na nudged to GEOS-5. Black dashed line: WACCM-Na nudged to MERRA. Blue dash-dotted line: Na lidar. The vertical dotted line marks a correlation coefficient of 0. Na lidar data have been averaged over six altitude bins (i.e. 900 m). (For interpretation of the references to color in this figure caption, the reader is referred to the web version of this article.)

coefficients calculated from lidar measurements, we have only selected altitudes at which we have at least 57 daily profiles (maximum number of measurements minus one standard deviation of measurements). In addition, we require the temperature
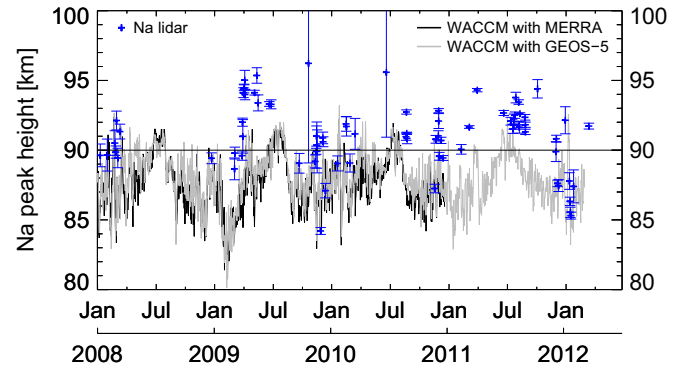
Fig. 7. Daily averages of the Na layer peak height in km. Grey solid line: Modelled peak height from WACCM-Na nudged to GEOS-5. Black solid line: Modelled peak height from WACCM-Na nudged to MERRA. Blue: peak height measured by Na lidar. The error bars indicate the 2σ range. (For interpretation of the references to color in this figure caption, the reader is referred to the web version of this article.)

uncertainty to 5 K or better. Above 95 km, the correlation coefficients are possibly influenced by tides and/or sporadic Na layers, even though sporadic layers are not a dominant feature in daily mean profiles. Sporadic Na layers are not included in WACCM-Na, so that differences between model and lidar data can, at least partly, be explained by these layers.

There is a small positive correlation between 80 and 90 km in the Na lidar data. Both WACCM-Na simulations have a larger positive correlation up to $R=0.85$ in that altitude range, peaking at 85.5 km. All three data sets show a decreasing correlation above 90 km, but in contrast to the models, the correlation of the Na lidar data does not become strongly negative. In both WACCM-Na runs, the correlation coefficient increases above 100 km, albeit remaining negative.

### 3.1.4. Na layer peak height and centroid height

The peak height of the sodium layer is the altitude of maximum density (i.e. peak density). Fig. 7 shows daily averages of the peak height for both lidar and WACCM-Na. The peak height measured by the Na lidar is mostly higher than the simulated peak height by WACCM-Na. On some occasions, however, all three data sets agree very well, most notably in the winter 2011/2012. The largest differences between lidar and model peak height are observed in summer months. The mean value ($\pm$ standard deviation) of the observed peak height by the Na lidar is (91.0 ± 2.4) km. The peak height simulated by WACCM(GEOS-5) is (88.1 ± 1.9) km, and (87.8 ± 1.9) km simulated by WACCM(MERRA).

The interplay of dynamics, chemistry, and meteoroid input governs the shape and strength of the sodium layer. Together with the peak height and peak density, the sodium layer's centroid height is a useful measure to characterise the layer properties. The centroid height z_c is computed according to the following equation:

$$z_c = \frac{\int_0^\infty n_{Na}(z) \cdot z \, dz}{\int_0^\infty n_{Na}(z) \, dz},$$

(2)

where $n_{Na}(z)$ is the Na number density at altitude z. The time series of diurnally averaged centroid height is plotted in Fig. 8.

The variability is slightly less than in the peak height data, but the same pattern is observed: the best agreement between lidar and WACCM-Na is in wintertime 2011/2012. The mean centroid height measured by the Na lidar (91.4 ± 1.5) km, and the simulated mean centroid height by WACCM-Na is (89.3 ± 1.1) km in both runs. The mean peak height is about 2–3 km higher in the Na lidar data compared to WACCM-Na. The difference in mean centroid heights is only slightly smaller, but still around 2 km higher in the
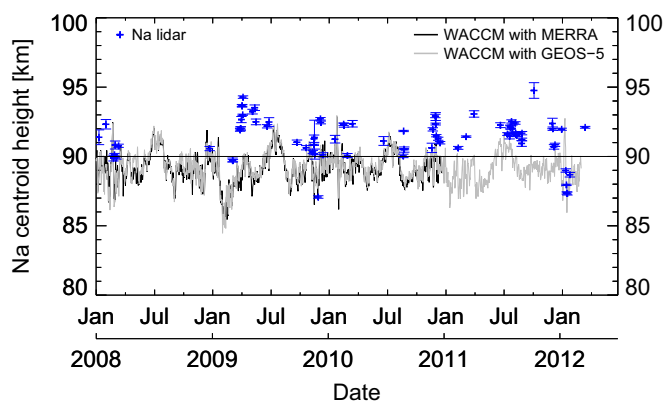
Fig. 8. Diurnal averages of the Na layer centroid height in km. Grey solid line: Modelled centroid height from WACCM-Na nudged to GEOS-5. Black solid line: Modelled centroid height from WACCM-Na nudged to MERRA. Blue: Centroid height measured by Na lidar. The error bars indicate the 2σ range. (For interpretation of the references to color in this figure caption, the reader is referred to the web version of this article.)

Na lidar data. On some days, the agreement of measured and modelled centroid and peak heights is very good, while on others the difference is larger, especially in summer. We have summarised the mean Na layer column density, peak density, peak height, and centroid height from both WACCM-Na runs and from the ALOMAR Na lidar in Table 3.

4. Discussion

We generally observe the best agreement between lidar observation and model simulations in winter. In summer, sodium densities are very low at high latitudes, and the sodium layer is narrower than in winter. This limits the altitude range in which temperature measurements can be made: in summer, these are possible between about 85 km and 95 km. The temperature measurements depend on the sodium densities: around the layer peak (~90 km to 95 km), temperature can be measured year-round, while measurements at 80 km and 100 km are only possible during winter. Compared to winter, measurements in summer have been sparse in most years. This is, to a large extent, due to overcast conditions.

Because of the comparably low Na densities above 100 km and below 83 km, the temperature uncertainties increase rapidly. Temperatures at 80.5 km and 101.5 km cannot always be measured, depending on the amount of sodium (i.e. the signal-to-noise ratio) present at these altitudes.

The uncertainty of the measured sodium densities by lidar is about 10%. However, this does not explain the rather large differences in the sodium column density between model and lidar. In wintertime, the Na column density is most often larger in WACCM-Na than in the lidar data by up to 50%. This could be evidence of too much convergence of Na atoms over the winter polar vortex, equal to what is seen at the South Pole (Marsh et al., 2013a). The high degree of convergence could be due to the meridional circulation in WACCM-Na being too strong, or the lifetime of the Na atoms being too long, such that they are transported over greater distances horizontally. A too strong meridional circulation appears to be consistent with warmer winter temperatures compared with the lidar data, see below.

The model and observations are consistent regarding the sudden stratospheric warming 2012. For the major sudden stratospheric warming 2009, Marsh et al. (2013a, Fig. 7) have shown that WACCM-Na simulated large variations in Na abundance over the polar cap. The WACCM-Na simulations also revealed temperature

variations of up to 50 K over the course of about ten days at the 0.002 hPa level (Marsh et al., 2013a, Fig. 8). The lidar measurements presented here (Fig. 3) confirm the model predictions of increased temperature and Na column density after the mesospheric cooling. Both the measurements and the model data show variations of the Na layer centroid height of about 4 km to 5 km. The influence of the solar proton event on 23/24 January 2012 is of minor importance, if any. This is subject to ongoing work.

The lidar data presented here confirm the model predictions in the case of the January 2012 stratospheric warming (Figs. 2– 5, 7). The quite substantial variations of both temperature and Na layer properties appear both in the model and in the measurements, and are in good agreement.

It is evident from Fig. 2(a) and (b) that the two WACCM-Na runs simulate different temperatures at higher altitudes, with WACCM (MERRA) being coldest. The difference is up to 7 K on average at 101.5 km, and decreases with decreasing altitude. At 92.5 km, both WACCM-Na simulations yield virtually equal mean temperatures (cf. Table 1). At 89.5 km and below, WACCM(MERRA) is slightly warmer than WACCM(GEOS-5).

As can be expected, the best agreement between average temperatures measured by Na lidar and simulated by WACCM-Na is found at the Na layer peak altitudes, i.e. between 89.5 km and 95.5 km, see Fig. 2(c)–(e). Rather large temperature differences of up to 50 K between lidar data and simulations do occur in autumn 2009, mostly at altitudes near the Na layer boundaries. There are several reasons for those differences. First, we compare a global three-dimensional model with a local lidar station. Second, the temperatures measured by lidar have uncertainties up to 15 K near the layer edges. Third, the temperatures measured by lidar are influenced by tidal and gravity waves. In the model, gravity waves are parameterised. Smith (2012, p. 1198) found that WACCM underestimates tidal amplitudes.

Average mesopause temperatures in winter are warmer by up to 10 K in the WACCM-Na simulations compared to lidar measurements, but the average mesopause altitude is approximately the same, especially when considering the vertical resolution of the data sets. The measured mesopause temperature in winter is somewhat colder than measured by Neuber et al. (1988), and the mesopause altitude is slightly lower.

The modelled peak and centroid heights, and the peak density agree to a certain extent with Na lidar measurements. Differences can be due to gravity waves and tides, which have an important influence on the measurements. In WACCM-Na, these processes are parameterised. Another reason is the at times rather short measurement duration, such that tidal influences are included in the measured data.

The seasonal cycle of high-latitude mesospheric Na densities is largely influenced by meridional transport (Gardner et al., 2005; Marsh et al., 2013a) and temperature. The stratospheric warming of January 2009 led to a pronounced perturbation of Na densities: at the onset, the Na density decreased by almost 50% to 4×10^{13} m^{-2}, followed by a large, rapid increase to about 1.5×10^{14} m^{-2}, which is very large even for winter. This temporal evolution is in very good agreement with polar cap (latitudes poleward of 70°N) averages shown by Marsh et al. (2013a, Figs. 7 and 8). They attribute the rapid decrease and subsequent increase to dynamics, not chemistry: meridional transport equatorwards led to the decrease of Na column density, followed by a convergence over the North Pole (Marsh et al., 2013a). Due to the relatively warm winter temperatures, the activation energy of the reaction NaHCO$_3$ + H → Na + H$_2$CO$_3$ (Plane, 2004, reaction (R9) in Table 1) is reached, leading to more atomic sodium. In summer, photo-ionisation leads to a reduced Na density on the topside of the Na layer, thus to a lower column density.

Another reason might be the value of the vertical eddy

diffusion coefficient k_{zz}, which is inversely proportional to the Prandtl number (Smith et al., 2011). The larger k_{zz}, the lower the Na density, whereas temperatures remain largely unaffected (Feng et al., 2013). The vertical eddy diffusion coefficient can be adjusted, but still it has to remain within certain boundaries. If the same meteoric input, Prandtl number, and velocity distribution are used, the modelled peak height of the Fe layer by WACCM-Fe (Feng et al., 2013) is in better agreement with observations than that of the Na layer.

The correlation (magnitude and sign) between Na number density and temperature (Fig. 6) can tell us which temperature-dependent rate coefficients in the atmospheric Na chemistry are important. Above about 95 km, where the model and the lidar data show a different behaviour, ion-molecule reactions dominate the Na chemistry (Plane et al., 1999). Plane (2002, and references therein) and Plane (2004) reported on the relevant ion-molecule reactions, of which only few are temperature-dependent. Of those, reaction (R29) given by Plane (2004) is the fastest, and shows a small temperature dependence (faster at colder temperatures):

$$Na. \, Y^+ + e^- \rightarrow Na + Y \, (Y = N_2, \, CO_2, \, H_2O, \, O)$$
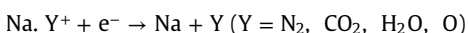
One possibility is that the Na chemistry is not yet fully understood. In the warm phase of tides, sporadic layers are often observed, such that a positive correlation seems possible, too. For the mid-latitude locations Fort Collins and Urbana-Champaign ($\sim$40°N), Plane et al. (1999) have found no significant correlation ($-0.3 < R < -0.1$) between measured Na number density and temperature at altitudes above 96 km. The positive correlation below 96 km is more pronounced at mid-latitudes (Plane et al., 1999) than in the results presented here (Fig. 6). At 69°N, the geophysical conditions (e.g. solar irradiation, auroral effects, or wave propagation) are different from those at lower latitudes, which might explain some of the differences.

5. Conclusions

We compare atmospheric temperatures, Na peak density, and Na column density observed by Na lidar on the one hand, and modelled with the Whole Atmosphere Community Climate Model on the other hand. The model results use two different datasets as boundary values: NASA's GEOS-5 and MERRA, respectively (the model is "nudged" to these datasets below 50 km). All parameters are usually compared as daily averages.

Overall, WACCM-Na reproduces very well the pronounced seasonal cycle of sodium densities and temperature. We observe the best agreement in winter months. The agreement between observations and simulations is especially good in all of 2011, and 2012. Considering the vertical resolution of model and lidar, the agreement is remarkable. Almost all values agree within the uncertainties and standard deviations when averages for the whole period are concerned.

The model predictions of substantial Na density and temperature variations during major stratospheric warming events are confirmed by Na lidar data for the January 2012 stratospheric warming.

Measured temperatures between 86.5 km and 95.5 km agree with WACCM-Na temperatures using GEOS-5 and MERRA as a boundary condition to within 10 K almost always. On a small percentage of measurement days ($< 20\%$), the observed temperatures at 92 km and above are warmer or colder than the model temperatures by as much as 30 K.

The correlation between Na number density and temperature is very different for WACCM-Na and for the Na lidar data. The WACCM-Na runs presented here are very similar to earlier results

obtained from WACCM-Fe, i.e. for iron instead of sodium (Feng et al., 2013). The correlation coefficient determined from Na lidar data at ALOMAR and from Fe lidar data at the South Pole differ in that the Na lidar does not show any pronounced negative correlation.

The assumed global meteoric input of Na ($0.035 \, \text{t} \, \text{d}^{-1}$) gives reasonable agreement with observations in WACCM-Na's chemistry scheme. Larger Na column densities simulated by WACCM-Na might be due to a too strong meridional circulation in the model, leading to larger convergence of sodium than is observed (Gardner et al., 2005, 2011). Variation of Na column density by a factor of up to ten or more appears in all three data sets with similar time constants. Model maxima and minima sometimes appear unsynchronised with observed maxima and minima. The modelled peak height, centroid height, and peak density all agree very well with measurements by the ALOMAR Na lidar.

From our comparison of two identical WACCM-Na simulations with different NASA reanalyses products (GEOS-5 and MERRA), we find that for upper mesospheric altitudes the two runs are very similar. It should be noted that the Na layer is not only temperature-dependent. Other dynamic and chemistry processes as well as the meteoroid input function also have a big impact on the layer. Given the good agreement of modelled Na, temperature for 69°N compared with lidar measurements, it should be noted the model chemistry (neutral and ionic) and dynamics (large meridional circulation, parameterisation of gravity waves) are still reasonable. There are also uncertainties regarding the rate constants of Na chemistry.

We plan to further analyse the stratospheric warming and the solar proton event in January 2012, using lidar and WACCM-Na data.

Acknowledgements

References

Arnold, K.S., She, C.Y., 2003. Metal fluorescence lidar (light detection and ranging) and the middle atmosphere. Contemp. Phys. 44 (1), 35–49.

Bowman, M.R., Gibson, A.J., Sandford, M.C.W., 1969. Atmospheric sodium measured by a tuned laser radar. Nature 221, 456–457.

Chandran, A., Collins, R.L., Harvey, V.L., 2014. Stratosphere-mesosphere coupling during stratospheric sudden warming events. Adv. Space Res. 53 (9), 1265–1289.

Chen, H., She, C.Y., Searcy, P., Korevaar, E., 1993. Sodium-vapor dispersive Faraday filter. Opt. Lett. 18 (12), 1019–1021.

Chen, H., White, M.A., Krueger, D.A., She, C.Y., 1996. Daytime mesopause temperature measurements with a sodium-vapor dispersive Faraday filter in a lidar receiver. Opt. Lett. 21 (15), 1093–1095.

Clemesha, B.R., Kirchhoff, V.W.J.H., Simonich, D.M., Takahashi, H., 1978. Evidence of an extraterrestrial source for the mesospheric sodium layer. Geophys. Res. Lett. 5 (10), 873–876.

Dunker, T., Hoppe, U.-P., Stober, G., Rapp, M., 2013. Development of the mesospheric Na layer at 69°N during the Geminids meteor shower 2010. Ann. Geophys. 31 (1), 61–73.

Feng, W., Marsh, D.R., Chipperfield, M.R., Janches, D., Höffner, J., Yi, F., Plane, J.M.C., 2013. A global atmospheric model of meteoric iron. J. Geophys. Res. -Atmos. 118

(16), 9456–9474.

Fricke, K.H., von Zahn, U., 1985. Mesopause temperatures derived from probing the hyperfine structure of the D_2 resonance line of sodium by lidar. J. Atmos. Terr. Phys. 47 (5), 499–512.

Gardner, C.S., Chu, X., Espy, P.J., Plane, J.M.C., Marsh, D.R., Janches, D., 2011. Seasonal variations of the mesospheric Fe layer at Rothera, Antarctica 67.5°S, 68.0°W. J. Geophys. Res. Atmos. 116 (D2), D02304.

Gardner, C.S., Plane, J.M.C., Pan, W., Vondrak, T., Murray, B.J., Chu, X., 2005. Seasonal variations of the Na and Fe layers at the South Pole and their implications for the chemistry and general circulation of the polar mesosphere. J. Geophys. Res. -Atmos. 110 (D10), D10302.

Gerding, M., Alpers, M., von Zahn, U., Rollason, R.J., Plane, J.M.C., 2000. Atmospheric Ca and Ca$^+$ layers: midlatitude observations and modeling. J. Geophys. Res. 105 (A12), 27131–27146.

Gibson, A.J., Thomas, L., Bhattacharyya, S.K., 1979. Laser observations of the ground-state hyperfine structure of sodium and of temperatures in the upper atmosphere. Nature 281 (5727), 131–132.

Harrell, S.D., She, C.Y., Yuan, T., Krueger, D.A., Chen, H., Chen, S.S., Hu, Z.L., 2009. Sodium and potassium vapor Faraday filters revisited: theory and applications. J. Opt. Soc. Am. B 26 (4), 659–670.

Heinrich, D., 2008. Temperature and sodium density studies in the Arctic mesopause region based on measurements with the ALOMAR Weber Sodium Lidar (Ph.D. thesis), University of Oslo.

Jackman, C.H., Marsh, D.R., Vitt, F.M., Garcia, R.R., Fleming, E.L., Labow, G.J., Randall, C.E., López-Puertas, M., Funke, B., von Clarmann, T., Stiller, G.P., 2008. Short- and medium-term atmospheric constituent effects of very large solar proton events. Atmos. Chem. Phys. 8 (3), 765–785.

Junge, C.E., Oldenberg, O., Wasson, J.T., 1962. On the origin of the sodium present in the upper atmosphere. J. Geophys. Res. 67 (3), 1027–1039.

Kaifler, B., 2009. Na Lidar at ALOMAR — electrooptic improvements, analysis algorithms and selected atmospheric observations 80 to 100 km above Northern Norway (Diploma thesis), Ulm University.

Kopp, E., 1997. On the abundance of metal ions in the lower ionosphere. J. Geophys. Res. 102 (A5), 9667–9674.

Lamarque, J.-F., Emmons, L.K., Hess, P.G., Kinnison, D.E., Tilmes, S., Vitt, F., Heald, C. L., Holland, E.A., Lauritzen, P.H., Neu, J., Orlando, J.J., Rasch, P., Tyndall, G., 2012. CAM-chem: description and evaluation of interactive atmospheric chemistry in CESM. Geosci. Model Dev. 5 (2), 369–411.

Lübken, F.-J., 1999. Thermal structure of the Arctic summer mesosphere. J. Geophys. Res. 104 (D8), 9135–9149.

Lübken, F.-J., von Zahn, U., 1991. Thermal structure of the mesopause region at polar latitudes. J. Geophys. Res. 96 (D11), 20841–20857.

Marsh, D.R., Janches, D., Feng, W., Plane, J.M.C., 2013a. A global model of meteoric sodium. J. Geophys. Res. Atmos. 118 (19), 11442–11452.

Marsh, D.R., Mills, M.J., Kinnison, D.E., Lamarque, J.-F., Calvo, N., Polvani, L.M., 2013b. Climate change from 1850 to 2005 simulated in CESM1 (WACCM). J. Clim. 26

(19), 7372–7391.

Matthes, K., Marsh, D.R., Garcia, R.R., Kinnison, D.E., Sassi, F., Walters, S., 2010. Role of the QBO in modulating the influence of the 11 year solar cycle on the atmosphere using constant forcings. J. Geophys. Res. Atmos. 115 (D18), D18110.

Neuber, R., von der Gathen, P., von Zahn, U., 1988. Altitude and temperature of the mesopause at 69°N latitude in winter. J. Geophys. Res. Atmos. 93 (D9), 11093–11101.

Nishikawa, T., Ozawa, A., Nishida, Y., Asobe, M., Hong, F.-L., Hänsch, T.W., 2009. Efficient 494 mW sum-frequency generation of sodium resonance radiation at 589 nm by using a periodically poled Zn:LiNbO$_3$ ridge waveguide. Opt. Express 17 (20), 17792–17800.

Plane, J.M.C., 2000. The role of sodium bicarbonate in the nucleation of noctilucent clouds. Ann. Geophys. 18 (7), 807–814.

Plane, J.M.C., 2002. Laboratory studies of meteoric metal chemistry. In: Murad, E., Williams, I.P. (Eds.), Meteors in the Earth's atmosphere. Cambridge University Press, Cambridge, UK, pp. 289–310, Ch. 12.

Plane, J.M.C., 2004. A time-resolved model of the mesospheric Na layer: constraints on the meteor input function. Atmos. Chem. Phys. 4 (3), 627–638.

Plane, J.M.C., 2012. Cosmic dust in the Earth's atmosphere. Chem. Soc. Rev. 41 (19), 6507–6518.

Plane, J.M.C., Gardner, C.S., Yu, J., She, C.Y., Garcia, R.R., Pumphrey, H.C., 1999. Mesospheric Na layer at 40°N: Modeling and observations. J. Geophys. Res. -Atmos. 104 (D3), 3773–3788.

Rienecker, M.M., Suarez, M.J., Gelaro, R., Todling, R., Bacmeister, J., Liu, E., Bosilovich, M.G., Schubert, S.D., Takacs, L., Kim, G.-K., Bloom, S., Chen, J., Collins, D., Conaty, A., da Silva, A., Gu, W., Joiner, J., Koster, R.D., Lucchesi, R., Molod, A., Owens, T., Pawson, S., Pegion, P., Redder, C.R., Reichle, R., Robertson, F.R., Ruddick, A.G., Sienkiewicz, M., Woolle, J., 2011. MERRA: NASA's modern-era retrospective analysis for research and applications. J. Clim. 24, 3624–3648.

Slipher, V.M., 1929. Emissions in the spectrum of the light of the night sky. Publ. Astronom. Soc. Pac. 41 (242), 262–263.

Smith, A.K., 2012. Global dynamics of the MLT. Surv. Geophys. 33 (6), 1177–1230.

Smith, A.K., Garcia, R.R., Marsh, D.R., Richter, J.H., 2011. WACCM simulations of the mean circulation and trace species transport in the winter mesosphere. J. Geophys. Res. -Atmos. 116 (D20), D20115.

von Zahn, U., von Cossart, G., Fiedler, J., Fricke, K.H., Nelke, G., Baumgarten, G., Rees, D., Hauchecorne, A., Adolfsen, K., 2000. The ALOMAR Rayleigh/Mie/Raman lidar: objectives, configuration, and performance. Ann. Geophys. 18, 815–833.

Vondrak, T., Plane, J.M.C., Broadley, S., Janches, D., 2008. A chemical model of meteoric ablation. Atmos. Chem. Phys. 8 (23), 7015–7031.

Yuan, T., She, C.Y., Krueger, D.A., Sassi, F., Garcia, R., Roble, R.G., Liu, H.-L., Schmidt, H., 2008. Climatology of mesopause region temperature, zonal wind, and meridional wind over Fort Collins (41°N, 105°W), and comparison with model simulations. J. Geophys. Res. -Atmos. 113 (D3), D03105.